Design Rules for Membranes from Polymers of Intrinsic Microporosity for Crossover-free Aqueous Electrochemical Devices

Citation: Miranda J. Baran et al. "Design Rules for Membranes from Polymers of Intrinsic Microporosity for Crossover-free Aqueous Electrochemical Devices." Joule, 3, 12 (December 2019): 2968–2985 © 2019 The Author(s)

As Published: 10.1016/J.JOULE.2019.08.025

Publisher: Elsevier BV

Persistent URL: https://hdl.handle.net/1721.1/127215

Version: Final published version: final published article, as it appeared in a journal, conference proceedings, or other formally published context

Joule

CellPress

Article

Design Rules for Membranes from Polymers of Intrinsic Microporosity for Crossover-free Aqueous Electrochemical Devices

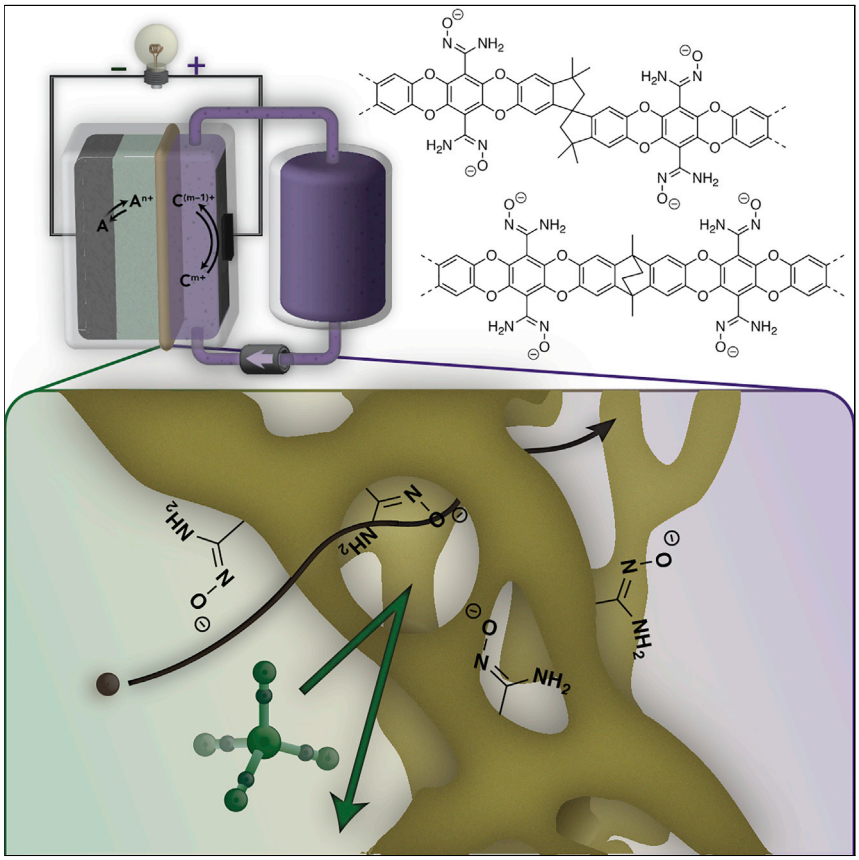

Placement of amidoxime functionalities within the pores of microporous polymer membranes yields a new family of selective membranes for aqueous electrochemical cells—which we call AquaPIMs. At high pH, where amidoximes are ionized, AquaPIM membranes feature concomitantly high conductivity and transport selectivity when compared to other membranes, including Nafion. Design rules are laid out, tying membrane architecture and pore chemistry to membrane stability, conductivity, and transport selectivity in aqueous electrolytes over a broad range of pH. These attributes dictate whether it is possible to operate aqueous electrochemical cells without the influence of active-material crossover.

Miranda J. Baran, Miles N. Braten, Swagat Sahu, ..., Yet-Ming Chiang, David Prendergast, Brett A. Helms

bahelms@lbl.gov

HIGHLIGHTS

Microporous polymer membranes with amidoximes are remarkably stable at high pH

Amidoxime membranes show high conductivity in alkaline electrolytes (21 mS cm^{-1})

Amidoxime membranes prevent the crossover of a wide range of active materials

A simple figure of merit predicts cell cycle life based on membrane selectivity

Baran et al., Joule 3, 2968–2985
December 18, 2019 Published by Elsevier Inc.
https://doi.org/10.1016/j.joule.2019.08.025

Joule

CellPress

Article

Design Rules for Membranes from Polymers of Intrinsic Microporosity for Crossover-free Aqueous Electrochemical Devices

Miranda J. Baran,[1,2] Miles N. Braten,[2] Swagat Sahu,[2] Artem Baskin,[2,3] Stephen M. Meckler,[1] Longjun Li,[2] Lorenzo Maserati,[2,3,4] Mark E. Carrington,[2,3] Yet-Ming Chiang,[5,6] David Prendergast,[2,3] and Brett A. Helms[2,3,7,8,*]

SUMMARY

Here, we lay the design rules for linking microporous polymer membrane architecture and pore chemistry to membrane stability, conductivity, and transport selectivity in aqueous electrolytes over a broad range of pH. We tie these attributes to prospects for crossover-free electrochemical cell operation. These guiding principles are applied to two emerging cell chemistries for grid batteries: specifically, Zn–TEMPO-4-sulfate and Zn–$K_4Fe(CN)_6$ cells. Key to our success is the placement of ionizable amidoxime functionalities, which are stable at high pH, within the pores of microporous ladder polymer membranes, yielding a family of charge-neutral and cation exchange membranes at low and high pH, respectively—which we call AquaPIMs. Their notably high conductivity (up to 21.5 mS cm^{-1} in 5.0 M aqueous KOH) and high transport selectivity (up to 10^4 reduction in active-material permeability through the membrane) suggest exciting opportunities for battery development, even beyond those presently demonstrated.

Context & Scale

The energy efficiency and cycle life of electrochemical cells with dissolved active materials are inextricably tied to the stability, conductivity, and transport selectivity of the cell's membrane. Membrane design rules have been lacking for such cells operating under harsh conditions, such as high alkalinity, due to the lack of selective, stable membranes. Here, we examined several classes of membranes for three aqueous Zn-based cell chemistries. In doing so, we uncovered a simple relationship between the membrane selectivity and the cell's cycle life, such that it is now possible to predict the lifetime of the cell on the basis of its membrane properties, thus avoiding time- or resource-intensive experimentation in large-format cells. Our work should greatly accelerate the identification of membranes for long-lasting, MW-scale redox-flow, and other low-cost grid batteries, which are required to last 10–20 years.

INTRODUCTION

The alkalinity of aqueous electrolytes used in many types of batteries, fuel cells, electrolyzers, and electrowinning apparatus is detrimental to the long-term stability of the membranes used in those devices.[1–3] Progressive degradation of organic functional groups at the molecular level leads to a reconfiguring of membrane pore architectures on meso- and macroscopic length scales, which in turn negatively impacts both working-ion conductivity and transport selectivity when using conventional polymer membranes.[4–6] This behavior is especially problematic for microporous polymer membranes, whose 0.5–2 nm pores and apertures have few opportunities to recover from even the subtlest structural deviations.[7]

Here, we show how to architect polymers comprising microporous membranes both to counteract this common failure mechanism and to present within the pores an ionizable and alkaline-stable functional group—the amidoxime ($pK_a \sim 13.3$)[8–10]—that imparts both high ionic conductivity and high transport selectivity in aqueous electrolytes (Figure 1). Within our architectural framework, we highlight the deterministic roles played by bridged bicyclic and spirocyclic monomers with varying contortion-site structure, in both 2D and 3D space (Figure 2), in obviating undesirable pore constriction at high pH.[11,12] These aqueous-compatible polymers of intrinsic microporosity—which we call AquaPIMs—deliver exceptionally stable

cation exchange membranes with tunable thickness (10–300 μm as stand-alone membranes; 0.5–200 μm as supported membranes) and high conductivity (up to 21.5 mS cm^{-1} in 5.0 M aqueous KOH) in aqueous electrolytes (pH 4.5–15) (Table S1). In addition, AquaPIM membranes selectively block active-material crossover relevant to a variety of energy storage devices, including Zn–Na 2,2,6,6-tetramethylpiperidine-*N*-oxyl-4-sulfate[13] (i.e., TEMPO-sulfate), Zn–$K_4Fe(CN)_6$,[14] and Zn–Na_2S_4[15] batteries. AquaPIMs' stability-conductivity-selectivity relationships contrast favorably with both non-selective mesoporous Celgard 3501 separators[16] and ion-selective Nafion 212 membranes,[17,18] indicating AquaPIMs are well positioned to offer substantive benefits to aqueous electrochemical cell performance, particularly for alkaline cell chemistries.

After evaluating cell performance for each of the aforementioned chemistries for cells configured with either AquaPIM, Nafion 212, or Celgard 3501 membranes, we found that capacity retention and, in turn, cycle life depended strongly on the ratio of the diffusion coefficient of the active material in solution (D_{sol}) to the diffusive permeability of the active material in the membrane (D_{eff}). Instances where $D_{sol}/D_{eff} > 10^3$ for both active materials in the cell (for membrane thicknesses 50–100 μm), capacity fade was slow and steady. For example, AquaPIM-enabled Zn–TEMPO-sulfate cells—where $D_{sol}/D_{eff} = 1.7 \times 10^3$ for $ZnCl_2$ and $D_{sol}/D_{eff} = 3.4 \times 10^4$ for TEMPO-sulfate—showed only 0.06% loss in capacity per cycle over 50 cycles (300 mA h capacity, cumulatively cycled over 13 days); cells configured with Nafion 212—where $D_{sol}/D_{eff} = 6.7 \times 10^1$ for $ZnCl_2$ and $D_{sol}/D_{eff} = 4.9 \times 10^2$ for TEMPO-sulfate—showed a 1.8% loss in capacity per cycle over 32 cycles (128 mA h capacity, cumulatively cycled over 5.7 days); cells configured with Celgard 3501—where $D_{sol}/D_{eff} = 2.1 \times 10^1$ for $ZnCl_2$ and $D_{sol}/D_{eff} = 2.3 \times 10^1$ for TEMPO-sulfate—showed a 3.9% loss in capacity per cycle over 14 cycles (30 mA h capacity, cumulatively cycled over 2.7 days). Similar observations were made in Zn–$K_4Fe(CN)_6$ cells for each membrane. Consistent with this analysis, instances where $D_{sol}/D_{eff} < 10^3$ for either active material in the cell, capacity fade was precipitous. For example, none of the membranes were effective in blocking polysulfide crossover in alkaline Zn–Na_2S_4 cells, where $D_{sol}/D_{eff} = 1.3 \times 10^2$, 6.7×10^1, and 7.8×10^0 are for AquaPIMs, Nafion, and Celgard, respectively. Thus, while AquaPIMs grant $D_{sol}/D_{eff} > 10^3$ for $Na_2Zn(OH)_4$ (i.e., zincate) and were demonstrably better at blocking polysulfide crossover than either Celgard 3501 or Nafion 212, ultimately it does not prevent the shortest polysulfide oligomers (e.g., Na_2S and Na_2S_2) from crossing over to the anode side of the cell, resulting in an ionically-insulating ZnS deposit on the Zn electrode that precludes Zn–Na_2S_4 cells from cycling.

The enabling character of AquaPIM membranes in Zn–TEMPO-sulfate and Zn–$K_4Fe(CN)_6$ cells is remarkable, indicating AquaPIMs and their variants are well poised to accelerate aqueous alkaline battery development, bringing back to the forefront low-cost and scalable battery chemistries that have otherwise been considered dead ends due to a lack of a selective and stable membrane under the extreme operating conditions of those cells. Furthermore, the design rules laid out here for linking membrane stability, conductivity, and transport selectivity to prospects for cell performance are also compelling. These experimentally validated guiding principles should accelerate the identification of ion-selective polymer membranes for the broad palette of emerging aqueous cell chemistries, including those based on inorganics,[15,19,20] metal coordination complexes,[14,21–23] organometallics,[24,25] polyoxometalates,[26–28] redox-active organic molecules,[13,25,29–36] and related macromolecular redoxmers.[37–44]

[1]Department of Chemistry, University of California, Berkeley, Berkeley, CA 94720, USA

[2]Joint Center for Energy Storage Research, Lawrence Berkeley National Laboratory, Berkeley, CA 94720, USA

[3]The Molecular Foundry, Lawrence Berkeley National Laboratory, Berkeley, CA 94720, USA

[4]Center for Nano Science and Technology@ PoliMi, Istituto Italiano di Tecnologia, Milano 20133, Italy

[5]Joint Center for Energy Storage Research, Massachusetts Institute of Technology, Cambridge, MA 02139, USA

[6]Department of Materials Science and Engineering, Massachusetts Institute of Technology, Cambridge, MA 02139, USA

[7]Materials Sciences Division, Lawrence Berkeley National Laboratory, Berkeley, CA 94720, USA

[8]Lead Contact

*Correspondence: bahelms@lbl.gov

https://doi.org/10.1016/j.joule.2019.08.025

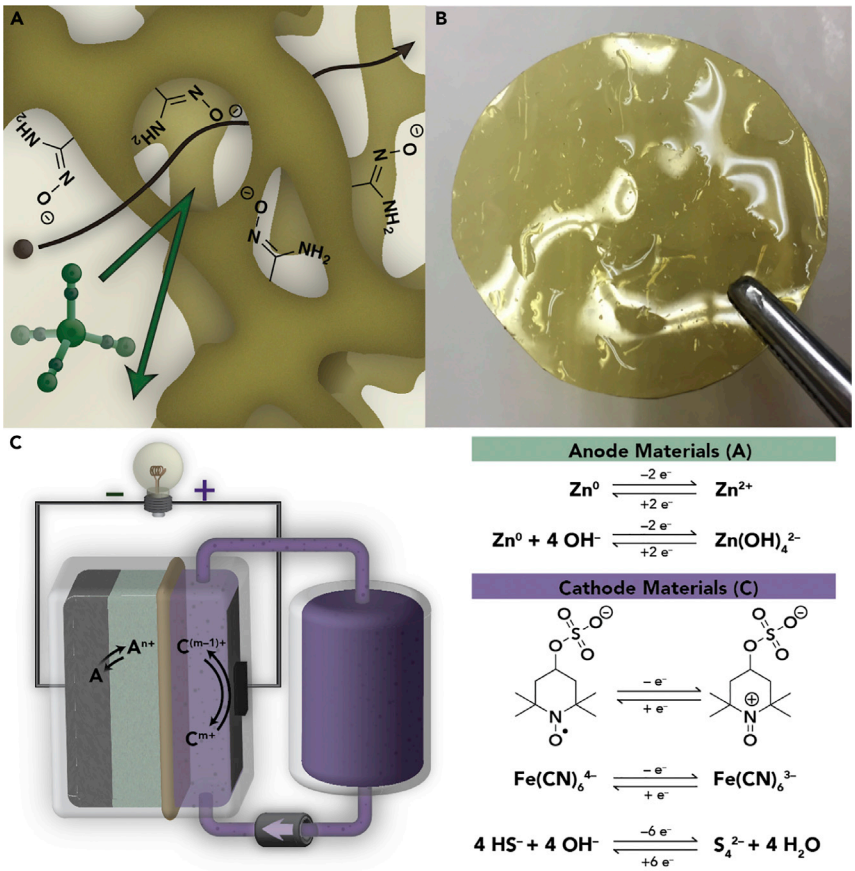

Figure 1. AquaPIM-Based Microporous Cation Exchange Membranes for Aqueous Alkaline Electrochemical Devices

(A) At high pH, amidoximes are ionized, yielding highly conductive and highly selective transport pathways in the membrane.

(B) AquaPIM membranes can be processed into a variety of formats, including the freestanding membrane shown, and are robust to handling in the dry and electrolyte-infiltrated state for pH > 4.5.

(C) Schematic of a hybrid redox-flow battery, where an ion-selective AquaPIM membrane allows crossover-free cell operation.

RESULTS AND DISCUSSION

Leveraging the Chemical Stability of Amidoximes and Structural Rigidity of Ladder Polymers to Counteract Membrane Degradation at High pH

Aqueous alkaline electrochemical cells present formidable challenges for membrane stability and conductivity as well as transport selectivity for active materials and working ions for a given cell chemistry.[3,45] With respect to stability, many organic functional groups (e.g., imides, benzimidazoles, quaternary ammoniums, phosphoniums, etc.) integrated into polymer membranes can be hydrolyzed or undergo elimination reactions at high pH.[5,6,46] Such chemical transformations are often deleterious to membrane performance. In most cases, the conductivity of the membrane will evolve with the extent of transformation, as will the transport selectivity. In extreme cases, the membrane's pores collapse, which has been attributed to unintended hydrogen bonding or ion pairing between complementary functional groups newly generated along the polymer backbone (e.g., carboxylate-ammonium bridges) or to changes in conformational and configurational entropy of the polymer backbone (e.g., due to benzimide or benzimidazole ring

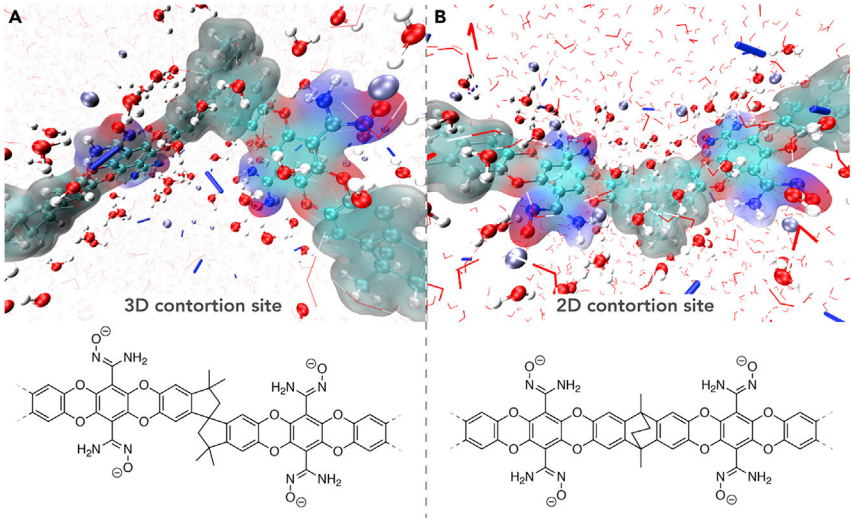

Figure 2. AquaPIM Backbone Structures at Contortion Sites

(A and B) Molecular representations of 3D (A) and 2D (B) AquaPIM contortion sites, with electrostatic surfaces denoted and the first solvation shells indicated with ball-and-stick water molecules.

opening).[47,48] Based on this understanding, we reasoned that alkaline-stable, ionizable functionality should be placed along the polymer backbone, rather than be a part of it, and that the backbone should have characteristically low conformational entropy (i.e., be endowed with structural rigidity) to avoid changes in packing across a broad range of pH or in response to adventitious chemical degradation. To meet the demands for working-ion conduction in many aqueous alkaline batteries, it is also desirable for the ionizable functionality to be anionic at high pH to afford cation exchange membranes.

To address the instability of chemical functionality appended to polymer backbones, used to promote membrane swelling and fast ion transport, we were drawn to the unique characteristics of amidoximes.[8,9] Amidoximes are polar and ionizable at both low and high pH (pK_{a1} ~4.5 and pK_{a2} ~13.3): at pH < 4, they are cationic; at pH 5–13, they are primarily charge-neutral; and at pH > 13, they are anionic (Figure 3A).[49,50] Such functionality grants expansive opportunities for cation exchange membrane development at high pH. Prior to our use of them as pore-lining chemical functionality in microporous polymer membranes for electrochemical devices, amidoxime-based polymeric materials have been previously implemented in gas separations[10] and in extracting lanthanides and actinides from processed ores, where their stability at pH > 13 is a strict requirement.[8,9,51]

To address the structural rigidity of the polymer backbone, we were drawn to an architectural platform based on ladder polymers, where conformational and configurational entropy are low and intrinsic microporosity can be high (10%–30%), relative to other classes of polymers (e.g., cellulosics, polysulfones, polyamides, polyimides, polyolefins, etc.). Such ladder polymers are often referred to as polymers of intrinsic microporosity (PIMs).[11,52,53] PIMs derive their unique sub-nm interconnected porosity from the frustrated packing of polymer chains in the condensed phase, which arises primarily from two macromolecular design characteristics: (1) severely restricted conformational degrees of freedom available to the polymer chain, through the incorporation of spirocyclic or polycyclic monomers into the main chain,

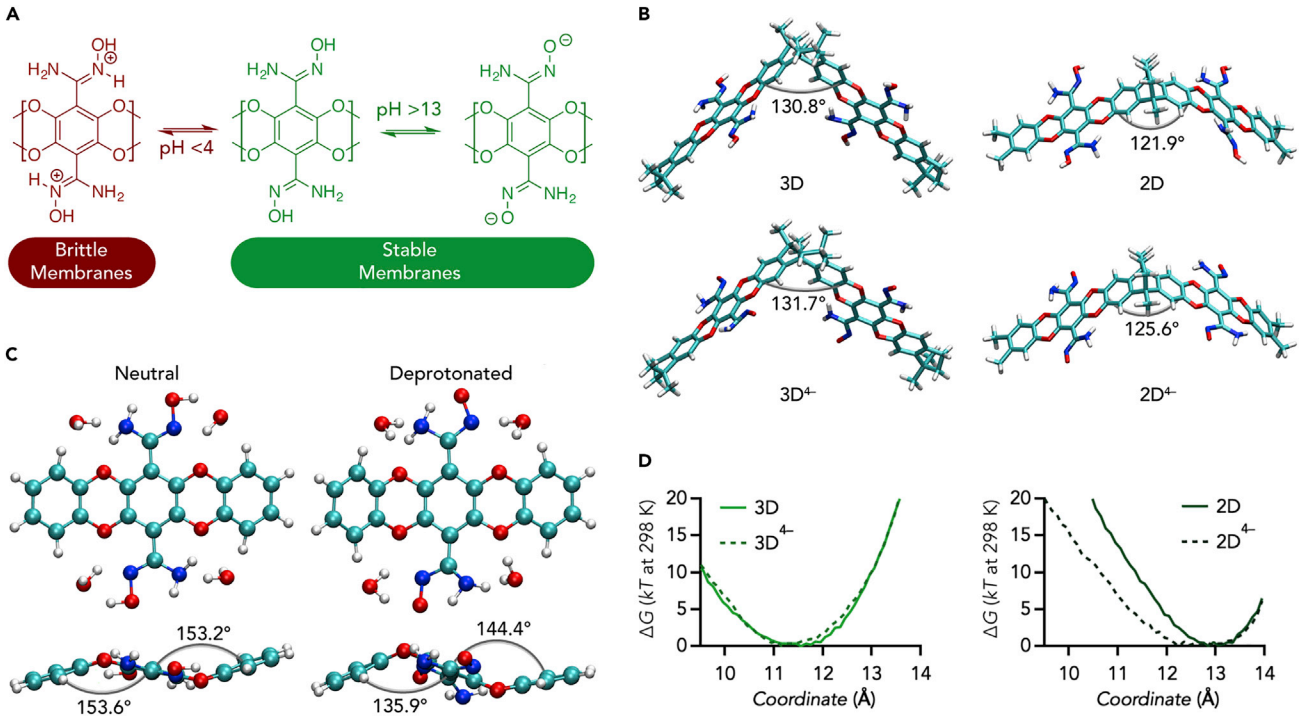

Figure 3. Leveraging the Chemical Stability of Amidoximes and Structural Rigidity of Ladder Polymers to Counteract Membrane Degradation at High pH

(A) Summary of AquaPIM membrane mechanical properties across the spectrum of pH commonly encountered in aqueous electrochemical cells.

(B) Optimal configurations from quantum mechanical calculations of 3D (spirocyclic) and 2D (bridged bicyclic) contortion sites showing that protonation state has a negligible impact on the contortion angle. See also Tables S2 and S3 for NBO charges.

(C) Configurations obtained from quantum mechanical calculations showing the effect of interactions between amidoximes and water on dibenzodioxane rigidity.

(D) Free-energy profiles of the 3D (spirocyclic) and 2D (bridged bicyclic) contortion sites in the neutral and fully deprotonated states. The "coordinate" refers to the distance between the centers of the two amidoxime-functionalized phenyl rings. See also Figure S1.

or alternatively, monomers whose bonds are hindered with respect to rotation (e.g., *ortho*-substituted arenes, atropisomers, etc.) and (2) persistent kinks along the main chain, in either 2D or 3D, depending on the nature of the site(s) of contortion embodied by the monomer(s).[2,10–12,41,52,54–57]

By appending ionizable and high-pH-stable amidoximes onto microporous ladder polymer backbones, we arrive at a family of AquaPIMs that serve effectively as ion-selective membranes in aqueous electrochemical devices. In this work, we advance the AquaPIM platform, revealing their foundational stability-conductivity-selectivity relationships for membranes that vary in the types and prevalence of both 2D and 3D contortion sites along the polymer backbone as well as the state of ionization of the amidoxime in aqueous electrolytes spanning pH 4.5–15, with the high-pH extreme consisting of 40% aqueous KOH (w/w). We contrast their behavior to two commercially available membranes: non-selective, mesoporous Celgard 3501 separators and ion-selective Nafion 212 membranes.

To demonstrate that the amidoxime functionality allows for the formation of stable pores under alkaline conditions, we explored the optimal structures of bridged bicyclic (2D) and spirocyclic (3D) dimers in various states of deprotonation and assessed the free-energy landscape for chain flexibility for both 2D and 3D contortion sites using quantum mechanical calculations and classical

molecular dynamics (Figure 3B, see Supplemental Information for details). Optimal configurations of these contortion sites (Figure 3B, variables illustrated in Figure S1 and longer polymer chains illustrated in Figure S2) show only subtle changes in backbone dihedral angles as a function of the state of deprotonation (~1° and ~4° for the spirocyclic and the bridged dimers, respectively). Both absolute dihedral angles and their changes with deprotonation are well reproduced in classical molecular dynamics simulations (Figure S3) with explicit consideration of a high pH (~2.3 M aqueous solution of NaOH). In the absence of ionic and dielectric screening, the center-of-mass separation of dimer branches increases, upon deprotonation, by ~3 Å (from 11.6 to 14.5 Å) and ~1 Å (from 13.2 to 14.4 Å) for the spirocyclic and the bridged bicyclic dimers, respectively (Figures 2B and S4). Additional quantum mechanical studies revealed flexibility of the dimer branches caused by changes in the electronic structures of the amidoxime groups induced by explicit, hydrogen-bonded water molecules (Figures 3C, S5, and S6). However, classical MD simulations show no significant changes of the average branch separations due to ionic screening (Figure S3). With the actual separation between the dimer branches being ~10 Å or more, at high pH, the centers of charge in the amidoxime groups are effectively decoupled due to the very short Debye screening length (<2 Å), which explains the insensitivity of the dimer structures to different states of deprotonation.

To understand the likelihood for pore network reconfigurability at different pH (and therefore degree of amidoxime ionization), we calculated the free energy as a function of center-of-mass separation of dimer branches for each dimer in the neutral and fully deprotonated states (Figure 3D). Due to the difference in the mutual orientation of the branches in the 2D and 3D dimers, the equilibrium separations are slightly different, yet largely independent of the degree of ionization. The curvatures of the free-energy profiles at the equilibrium separations reflect the overall softness of dimers, mostly related to the bending of the dimer branches. To change the equilibrium separation between branches by $\sim \pm 1.5$ Å requires $\sim 10\, k_B T$ of free energy at room temperature; however, we find that further changes require modification to the dihedral angles at the contortion sites, making such changes highly unlikely. As a result, the proposed polymer structures are predicted to be sufficiently rigid to maintain porosity under both neutral and highly alkaline conditions.

To explore the impact of a given monomer's contortion-site geometry and occurrence on the properties of AquaPIM membranes, we synthesized amidoxime-functionalized AquaPIMs **1–3** using a high-yielding, scalable two-step sequence (Figure 4A). Here, tetrafluoroterephthalonitrile was polymerized under basic conditions in DMF with varying proportions of bridged bicyclic and spirocyclic biscatechol monomers, which feature 2D and 3D contortion sites, respectively. Then, we interconverted the cyano groups on the polymers, quantitatively, to amidoximes using hydroxylamine under refluxing conditions, yielding AquaPIMs **1–3**.[10] While AquaPIMs **1–3** were soluble polymers, suitable for casting membranes, those incorporating more than 50% of the bridged bicyclic monomer were not immediately; therefore, we restricted our analysis to these three.

To understand the pore-size distribution of AquaPIMs **1–3**, we collected N_2 (Figure 4C) and CO_2 (Figure S7) adsorption isotherms. Pronounced N_2 adsorption at low pressure reveals intrinsic microporosity (pores < 20 Å) in all three polymers. Non-local density functional theory (NLDFT) pore-size distributions fit to these data reveal how the spirocyclic and bridged bicyclic biscatechol residues direct pore architecture. When exclusively spirocyclic residues are present in AquaPIM **1**,

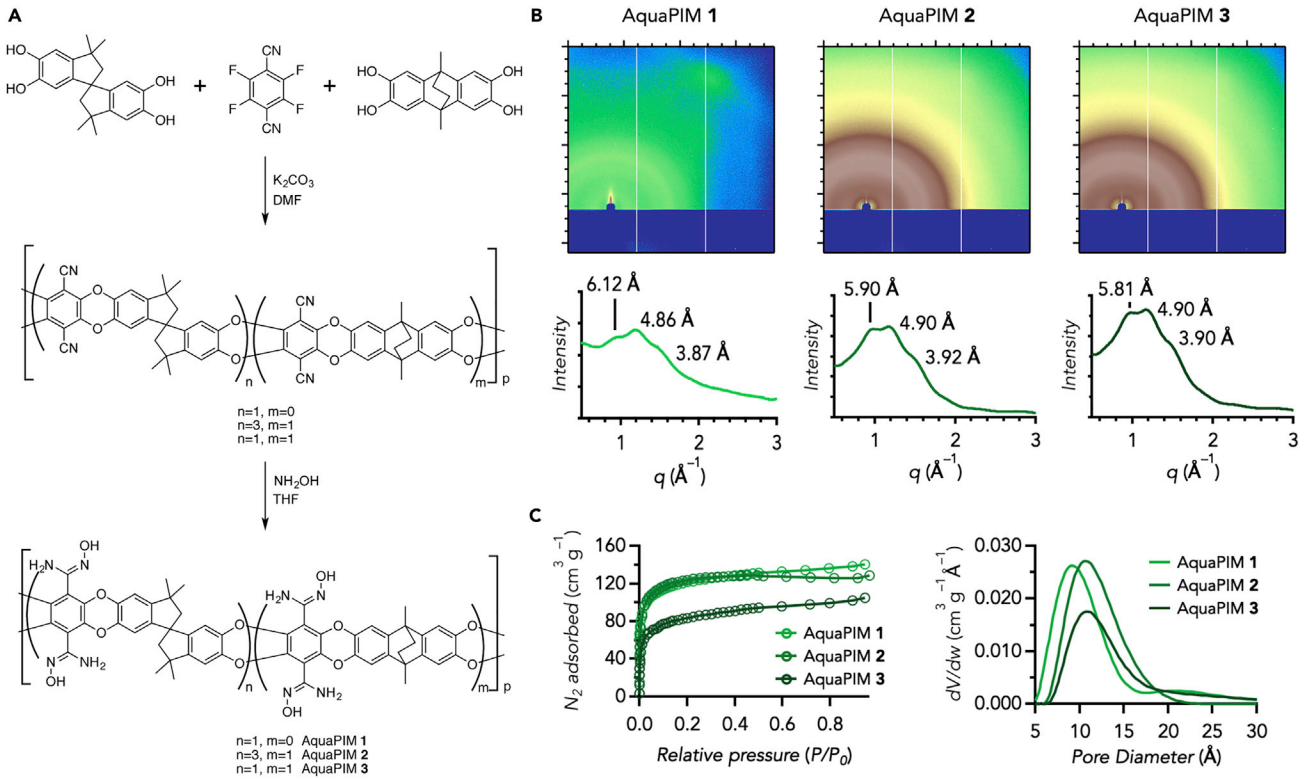

Figure 4. Differentiating the Architectural Attributes of AquaPIM Membranes on the Basis of the Prevalence of 2D and 3D Contortion Sites along the Polymer Backbone

(A) Synthetic scheme for the synthesis of AquaPIMs **1–3**. The proportion of spirocyclic and bridged bicyclic biscatechol monomers are varied to diversify the membrane pore architectures. Notably, the amidoxime functionality is introduced in a quantitative, post-polymerization modification.

(B) Grazing-incidence wide-angle X-ray scattering of AquaPIMs **1–3**.

(C) Nitrogen adsorption isotherms and pore-size distributions for AquaPIMs **1–3**. Pore-size distributions are modeled from the adsorption data using NLDFT.

a high surface area of 454 $m^2\ g^{-1}$ and pores approximately 8.6 Å wide are observed. As bridged bicyclic residues are introduced into the polymer backbone in AquaPIM **2**, we see an increase in pore size to 10.5 Å, while the surface area is very similar (472 $m^2\ g^{-1}$). Further increasing the proportion of bridged bicyclic residues into AquaPIM **3** leads to a loss of surface area (309 $m^2\ g^{-1}$), without any change in pore size (10.5 Å pores). Ultra-microporosity (pores < 7 Å) is also observed in the gas uptake in the low-pressure regions of the CO_2 isotherms, which show similar porosity for all three polymers in this size regime, at ~5.6 Å.

Further investigation of the pore structure was undertaken using grazing-incidence wide-angle X-ray scattering (GIWAXS) before (Figure S8) and after (Figure 4B) the introduction of the amidoxime functionality.[58] Prior studies on PIM wide-angle X-ray scattering (WAXS) patterns indicate that a broad, low-q scattering feature peaking below 0.5 $Å^{-1}$ is indicative of microporosity.[59,60] A broad scattering feature at $q \sim 1–1.1\ Å^{-1}$ (4.9–6.1 Å in real space) is observed for AquaPIMs **1–3**. By comparison, hydrophobic PIMs **1–3** exhibit a scattering feature at $q \sim 0.6\ Å^{-1}$ (9.8–10.8 Å in real space) as well as peaks at larger q, which track those observed for the AquaPIMs. The lack of low-q intensity in the AquaPIM scattering patterns suggests that the polymer network is more densely packed than some other PIMs, which is expected given the hydrogen bond accepting and donating nature of amidoxime groups. This

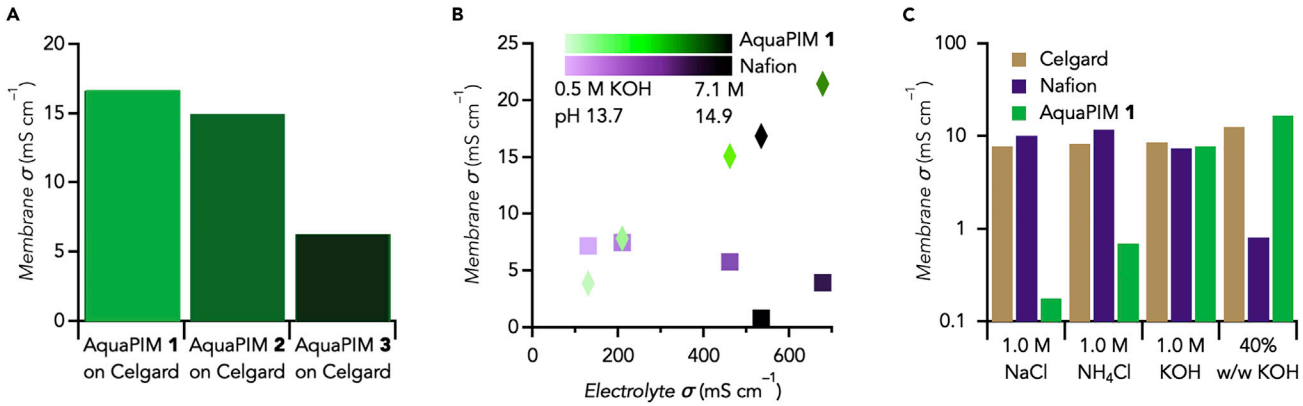

Figure 5. Impact of Membrane Pore Architecture on Ionic Conductivity in Highly Alkaline Aqueous

Electrolyte for AquaPIMs 1–3 and Differentiating Electrolyte-Conductivity Relationships for AquaPIM 1 Membranes alongside Celgard 3501 and Nafion 212.

(A) Membrane ionic conductivity (σ) for AquaPIMs **1–3** supported on Celgard 3501 as measured in 40% aqueous KOH (w/w).

(B) Membrane ionic conductivity (σ) for freestanding AquaPIM **1** as measured in 0.5, 1.0, 2.5, 5.0, and 7.1 M aqueous KOH.

(C) Membrane ionic conductivity (σ) for freestanding AquaPIM **1** as measured in 1.0 M NaCl, 1.0 M NH_4Cl, 1.0 M KOH, and 40% aqueous KOH (w/w), relative to mesoporous Celgard 3501 and Nafion 212 membranes.

See also Figures S13–S16 for associated Nyquist plots, and Tables S4 and S5 for a summary of resistance, conductivity, and ASR data.

microstructural analysis of the pore network is consistent with that obtained from the N_2 adsorption experiments.[61]

The architectural attributes for AquaPIMs **1–3** take form as a microporous polymer membrane for aqueous electrochemical devices by solvent casting since the T_g for PIMs is higher than their temperature of decomposition (i.e., PIMs are not thermally processable).[62] We prepared both freestanding and supported membranes using solvent-casting techniques from inks formulated in *N*-methyl-2-pyrrolidone (100–300 mg mL^{-1}). Of the three polymers, membranes cast from AquaPIM **1** were the most robust to handle a wide range of electrolyte formulations and membrane thicknesses, on or off a support such as Celgard 3501. We noted that membranes from AquaPIMs **1–3** were brittle after equilibration in harshly acidic electrolytes (pH < 4), while under mildly acidic (1.0 M NH_4Cl, pH 4.5) to extreme alkaline (40% w/w KOH) conditions, the membranes were handled easily (see Figures S9–S12 for in-depth characterization of mechanical and chemical stability as well as electrolyte uptake). Hydrogen bonding preferences for pendant amidoximes at various states of ionization are likely responsible for the observed differences in brittleness (Figure 3A). To confirm the chemical stability of the polymer membranes after equilibration in highly alkaline media, we conducted Fourier transform infrared (FTIR) and ^1H NMR spectroscopic analysis for each membrane (Figure S11), noting strikingly similar spectral features for membranes soaked in either deionized water or 40% aqueous KOH (w/w).

Ionizability of Amidoximes at High pH Amplifies the Ionic Conductivity of AquaPIM Membranes

To quantify the membrane ionic conductivity for AquaPIMs **1–3** in highly alkaline aqueous electrolyte, we equilibrated supported membranes in 40% aqueous KOH (w/w) and assembled them in custom-purposed Swagelok cells without additional electrolyte. Analysis of the Nyquist plots obtained by electrochemical impedance spectroscopy (EIS) of these cells (Figure S13A) allowed for the resistance of the AquaPIM overlayer to be extracted, after subtracting the contribution from the underlying Celgard 3501 support (Figure 5A). The intrinsic membrane ionic

conductivity was then calculated by considering the thickness of the AquaPIM overlayer: σ values of 16.7, 15.0, and 6.3 mS cm^{-1} differentiated the transport properties of AquaPIMs **1–3**, respectively. The observed changes were consistent with the relative pore architecture of the three polymers (Figure 4C), which are evidently dictated by the ratio of 2D and 3D monomers incorporated into the polymer chains. While all three polymers exhibited high conductivity under these conditions, we advanced AquaPIM **1** as the most promising for direct comparison to other membranes, considering their ease of processability and superior mechanical integrity.

The ionic conductivity of AquaPIMs **1–3** in aqueous alkaline electrolyte is on par or higher when compared to other polymer membranes, however, most of these membranes have been developed as anion-exchange membranes for fuel cells and other devices[18,63–70] The intentional design of AquaPIMs as cation exchange membranes begins to resolve technology gaps for polymer membranes suitable for use in aqueous alkaline electrochemical devices, where the working ions may be cations rather than hydroxide or chloride. This led us to further consider the foundations for ion transport by AquaPIM **1** in other aqueous electrolytes, by varying the chemical identity of the supporting salt as well as pH, all of which influence the extent of ionization of the amidoxime and in turn the structure and dynamic properties of water and ions confined to amidoxime-lined pores at the sub-nm scale. The ionic conductivity for freestanding AquaPIM **1** membranes (~100 μm) was evaluated for infiltrating electrolytes consisting of 1.0 M NaCl, 1.0 M NH_4Cl, 0.5 M KOH, 1.0 M KOH, 2.5 M KOH, 5.0 M KOH, and 40% aqueous KOH (w/w) (Figures 5B and 5C) from Nyquist plots obtained by EIS as described above (Figures S14 and S15). These data were also acquired for Celgard 3501 separators as well as Nafion 212 membranes for comparison. For mesoporous Celgard 3501, which wets but does not swell in aqueous electrolytes, we showed a monotonic increase in the separator ionic conductivity with increasing ionic conductivity of the electrolyte, as expected. On the other hand, for Nafion 212, there is an initial increase in membrane ionic conductivity with increasing electrolyte ionic conductivity (i.e., for 1.0 M NaCl, 1.0 M NH_4Cl, and 1.0 M KOH electrolytes) but also a notable decrease in conductivity when infiltrated with alkaline electrolytes (see Figures 5B and S16). Our determinations of the membrane ionic conductivity of Nafion 212 in aqueous alkaline electrolytes are consistent with measurements elsewhere.[71]

There have been several explanations postulated for the observed behavior with Nafion 212 in alkaline electrolytes: the partitioning of ions in the electrolyte does not track the bulk electrolyte for high KOH concentrations; the increased ionic strength more effectively screens the repulsive interactions between the perfluoroalkylsulfonates, constricting the membrane's pores; the dynamics of water and ions in the pores are comparably slow for concentrated liquid electrolytes; or the low degree of phase separation in the KOH, resulting in fewer regions of high hydrophilicity to allow for ion shuttling.[4,71–74] Contrasting this behavior, AquaPIM **1** membranes exhibit their highest membrane ionic conductivity for electrolytes whose pH is greater than the pK_a of the amidoxime (Figures 5B and 5C). Thus, while AquaPIM **1**'s membrane ionic conductivity is 0.18 mS cm^{-1} for the 1.0 M NaCl electrolyte and 0.70 mS cm^{-1} for the 1.0 M NH_4Cl electrolyte, its conductivity jumps orders of magnitude to 7.9 mS cm^{-1} for the 1.0 M KOH electrolyte and advances further to 21.5 mS cm^{-1} at 5.0 M KOH and eventually backtracks to 16.9 mS cm^{-1} in 40% aqueous KOH (w/w) due to its higher viscosity. AquaPIM conductivity therefore quickly meets and eventually exceeds that of Nafion 212 with increasing KOH in the electrolyte. The resilience of AquaPIM **1** membranes to both high pH and high ionic strength suggests more effective partitioning of ions from the concentrated

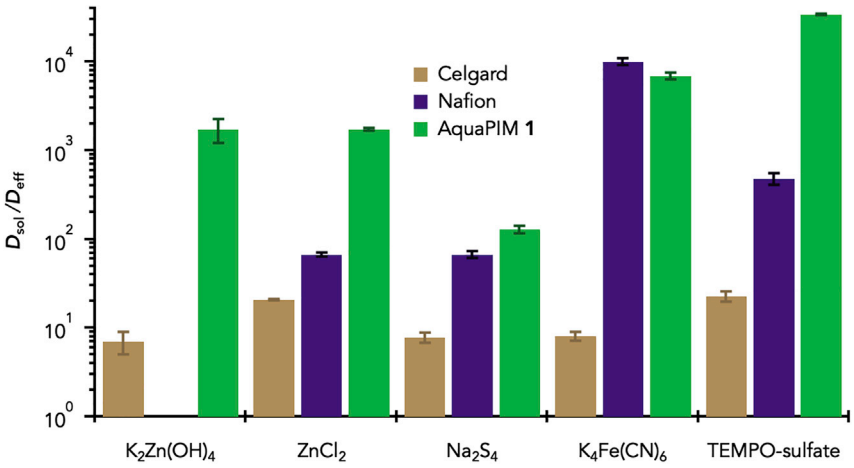

Figure 6. Quantifying the Extent to which AquaPIM 1, Celgard 3501, and Nafion 212 Membranes Restrict the Diffusive Transport of Various Battery Active Materials in Aqueous Electrolytes

Higher ratios for a given active material's diffusive permeability in the membrane (D_{eff}) to its diffusion in electrolyte (D_{sol}) indicate better blocking by a given membrane. AquaPIM **1** outperforms both commercial membranes for most active materials, often by orders of magnitude for this figure of merit.

See also Table S6 for a summary of diffusion coefficients and Figures S18–S23 for calibration curves and crossover measurements.

liquid electrolyte into the membrane's network of pores, less pore constriction, and more favorable dynamics of water and ions in the pore network compared to Nafion 212. This further indicates that sub-nm porous AquaPIM **1** membranes may be well-suited to serve as membranes in aqueous electrochemical devices requiring high conductivity and high transport selectivity for working ions over active materials.

Sub-nanometer Pore Architectures Inherent to AquaPIM Membranes Strictly Enforce Membrane Transport Selectivity

A variety of cell chemistries based on inorganics, metal coordination complexes, organometallics, polyoxometalates, and redox-active organic molecules have recently emerged, setting the stage for membrane development, given the challenges faced in managing active-material crossover in cells implementing them.[20–22,29] As an initial survey of opportunities, we focused on three cell chemistries: Zn–TEMPO-sulfate, Zn–$K_4Fe(CN)_4$, and Zn–Na_2S_4.[13–15] We evaluated the extrinsic rates of crossover for $K_2Zn(OH)_4$ (i.e., zincate), $ZnCl_2$, Na_2S_4 (i.e., polysulfides), $K_4Fe(CN)_4$, and sodium TEMPO-4-sulfate (i.e., TEMPO-sulfate) using a diffusion cell equipped with either AquaPIM **1**, Nafion 212, or Celgard 3501 membranes (Figures S17–S23). From these data, we then calculated their intrinsic diffusive permeability in each membrane (D_{eff}). To compare the blocking properties for each active material, D_{eff} values were normalized to the diffusion coefficient of the actives in electrolyte (D_{sol}), which were separately determined by cyclic voltammetry (Figures 6 and S17). Higher values for D_{sol}/D_{eff} indicate better active-material blocking by the membrane in a given electrolyte.

Notably, AquaPIM **1** membranes give D_{sol}/D_{eff} of 1.7×10^3 for both zincate and $ZnCl_2$, thereby more effectively managing crossover than either Nafion 212 ($D_{sol}/D_{eff} = 6.7 \times 10^1$ for $ZnCl_2$) or Celgard 3501 ($D_{sol}/D_{eff} = 7.1 \times 10^0$ and 2.1×10^1 for zincate and $ZnCl_2$, respectively). For the catholytes, differentiating the blocking ability by the membranes was subtler. AquaPIM **1** gave the highest

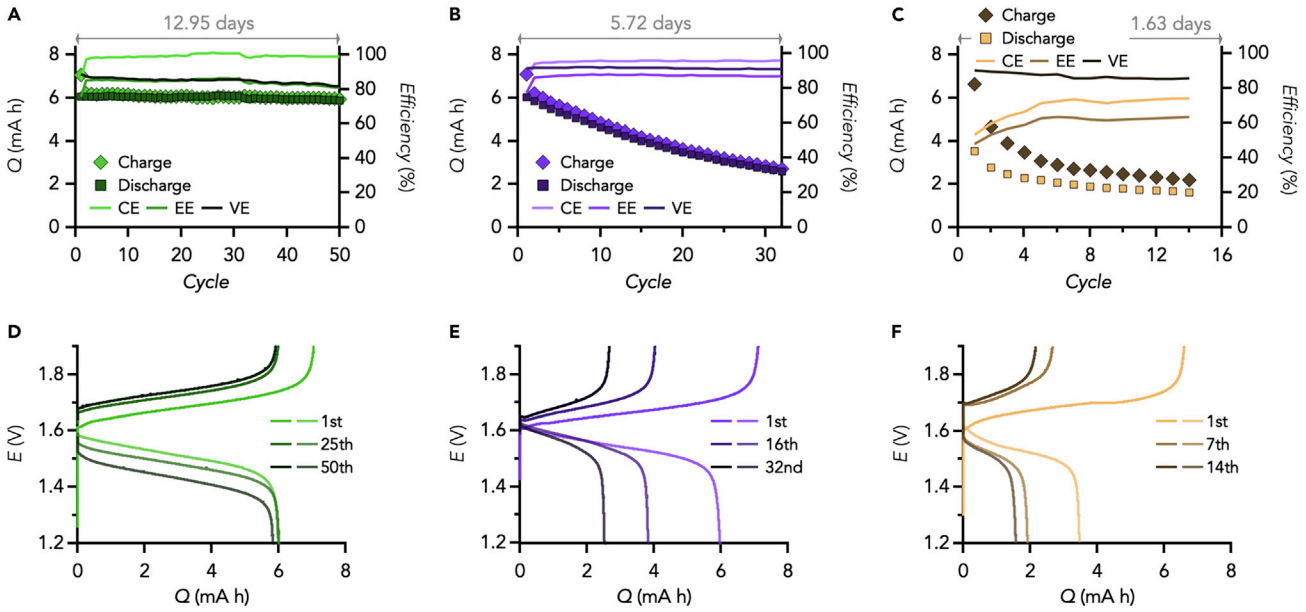

Figure 7. Differentiating the Performance of Zn–TEMPO-Sulfate Batteries Configured with AquaPIM 1, Nafion 212, or Celgard 3501 Membranes

(A–C) Charge and discharge capacity (*Q*) with corresponding Coulombic efficiency (*CE*), energy efficiency (*EE*), and voltage efficiency (*VE*) for Zn–TEMPO-Sulfate cells configured with either (A) AquaPIM **1**, (B) Nafion 212, or (C) Celgard 3501 membranes. Theoretical capacity = 8 mA h.

(D–F) Charge and discharge curves of the first, intermediate, and last cycles for Zn–TEMPO-Sulfate cells configured with either (D) AquaPIM **1**, (E) Nafion 212, or (F) Celgard 3501 membranes.

See also Figures S24–S26 and S30 for additional cycling data and (electro)chemical analyses of the membranes and electrolytes before and after cycling.

D_{sol}/D_{eff} of all of the active materials explored for TEMPO-sulfate (D_{sol}/D_{eff} = 3.4 × 10^4), outperforming by orders of magnitude Nafion 212 (D_{sol}/D_{eff} = 4.9 × 10^2) and Celgard 3501 (D_{sol}/D_{eff} = 2.3 × 10^1). However, for $K_4Fe(CN)_4$, AquaPIM **1** and Nafion 212 were comparable and high— D_{sol}/D_{eff} = 1.0 × 10^4 and 6.9 × 10^3, respectively— with both outperforming Celgard 3501 (D_{sol}/D_{eff} = 8.2 × 10^0). Finally, for Na_2S_4, crossover was only modestly managed by AquaPIM **1** and Nafion 212 under highly alkaline conditions, with both outperforming Celgard 3501: D_{sol}/D_{eff} = 1.3 × 10^2, 6.7 × 10^1, and 7.8 × 10^0, respectively.

AquaPIM Membrane Stability, Conductivity, and Transport Selectivity Dictate Prospects for Crossover-free Cell Operation

We next set out to determine how D_{sol}/D_{eff} for a given membrane, electrolyte, and pair of active materials for anolyte and catholyte, in turn, dictate key aspects of aqueous cell performance, including accessible capacity, Coulombic efficiency, and cycle life (Figures 7 and 8). Given the high D_{sol}/D_{eff} for both $ZnCl_2$ and TEMPO-sulfate for AquaPIM **1** in 1.0 M NH_4Cl electrolyte, we hypothesized that Zn–TEMPO-sulfate cells (~1.70 V) would perform best with the AquaPIM **1** membrane in place. To test this hypothesis, we assembled 8 mAh-capacity Zn–TEMPO-sulfate cells (Figure 7) consisting of a Zn anode, a 0.50 M $ZnCl_2$ anolyte in 1.0 M NH_4Cl, any one of the three membranes under consideration, a 35 mM TEMPO-sulfate catholyte in 1.7 M NH_4Cl, and a reticulated vitreous carbon current collector. All cells were cycled at 25°C at a rate of C/4. Both AquaPIM **1** and Nafion cells accessed ~75% of the theoretical capacity in the first cycle; however, non-selective Celgard 3501 only accessed 44%. Thereafter, the AquaPIM **1** cell maintained 97% of its initial capacity after 50 cycles over ~13 days (0.06% loss per cycle) with Coulombic efficiencies steady at ~99%. On the other hand, for Nafion 212 and Celgard 3501 cells, after the first cycle, we noted rapid capacity fade for both: Nafion

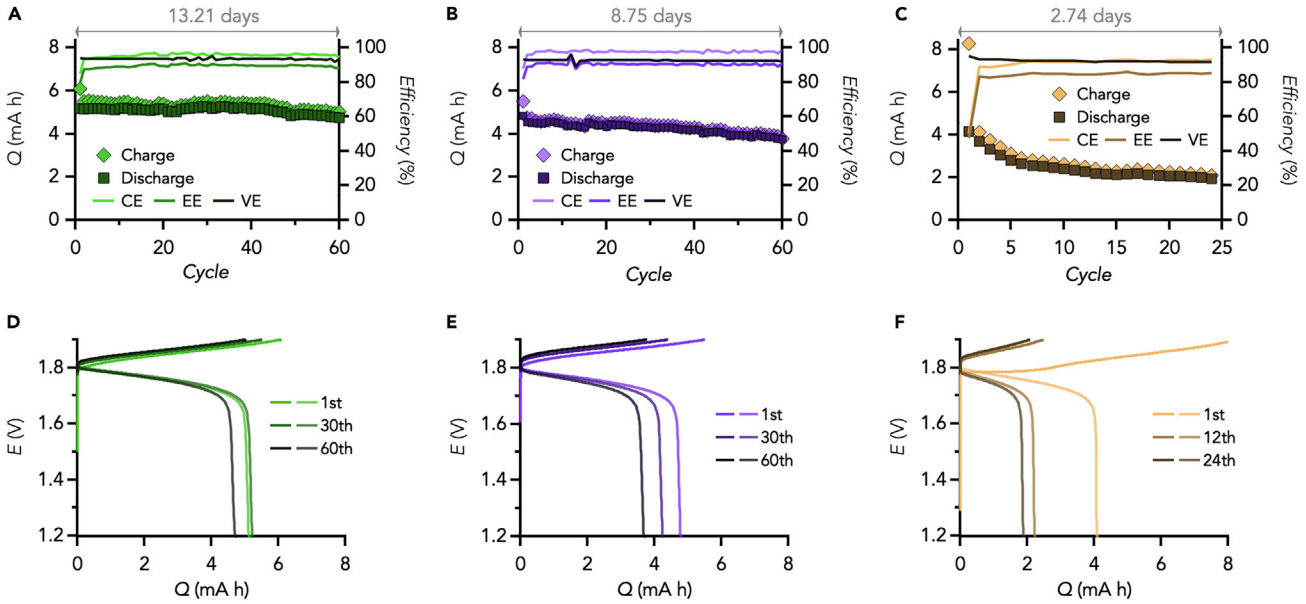

Figure 8. Differentiating the Performance of Zn–$K_4Fe(CN)_6$ Batteries Configured with AquaPIM 1, Nafion 212, or Celgard 3501 Membranes

(A–C) Charge and discharge capacity (*Q*) with corresponding Coulombic efficiency (*CE*), energy efficiency (*EE*), and voltage efficiency (*VE*) for Zn–$K_4Fe(CN)_6$ cells configured with either (A) AquaPIM **1**, (B) Nafion 212, or (C) Celgard 3501 membranes. Theoretical capacity = 8 mA h.

(D–F) Charge and discharge curves of the first, intermediate, and last cycles for Zn–$K_4Fe(CN)_6$ cells configured with either (D) AquaPIM **1**, (E) Nafion 212, or (F) Celgard 3501 membranes, respectively.

See also Figures S27–S30 for additional cycling data and (electro)chemical analyses of the membranes and electrolytes before and after cycling.

212 retained only 43% of its initial capacity after 34 cycles over 5.7 days (~1.8% loss per cycle) with Coulombic efficiencies steady at ~95%, and Celgard 3501 retained only 46% over 13 cycles over 1.6 days (~3.9% loss per cycle) with Coulombic efficiencies of 50%–70%. We tied either the retention or loss in cell capacity to TEMPO-sulfate crossover. Specifically, analysis of the anolytes after cycling revealed that TEMPO-sulfate did not crossover for cells equipped with AquaPIM **1**, while crossover was rampant for Nafion 212 and Celgard 3501 (Figure S25).

To make explicit the correlation between active-material permeability across the membranes and cell performance, we plotted the Coulombic inefficiencies multiplied by the inverse of the cumulative cycle time of the cells against either the absolute permeability[75] or D_{sol}/D_{eff} for each active material and membrane (Figure 9). From these plots, it is evident that high Coulombic inefficiencies and short cycle lives are strongly and inversely correlated with membrane permeability for $ZnCl_2$ and TEMPO-sulfate, confirming our hypothesis. We further concluded that cells for which $D_{sol}/D_{eff} \sim 10^3$ for both active materials granted crossover-free operation, yielding longer cycle life and higher Coulombic efficiency, as evidenced by the superior performance of Zn–TEMPO-sulfate cells with AquaPIM **1** membranes in place.

To further demonstrate that $D_{sol}/D_{eff} > 10^3$ for a given membrane, electrolyte, and pair of active materials for anolyte and catholyte grants stable, crossover-free aqueous cell performance, we turned our attention to the demonstrably high $K_2Zn(OH)_4$ and $K_4Fe(CN)_6$ blocking ability by AquaPIM **1** and Nafion 212 membranes in 40% aqueous KOH (w/w). However, it should be noted that poor conductivity, owing to reduced phase separation, in part, prevented an accurate determination of D_{sol}/D_{eff} for zincate by Nafion 212 in our hands. Nevertheless, based on their

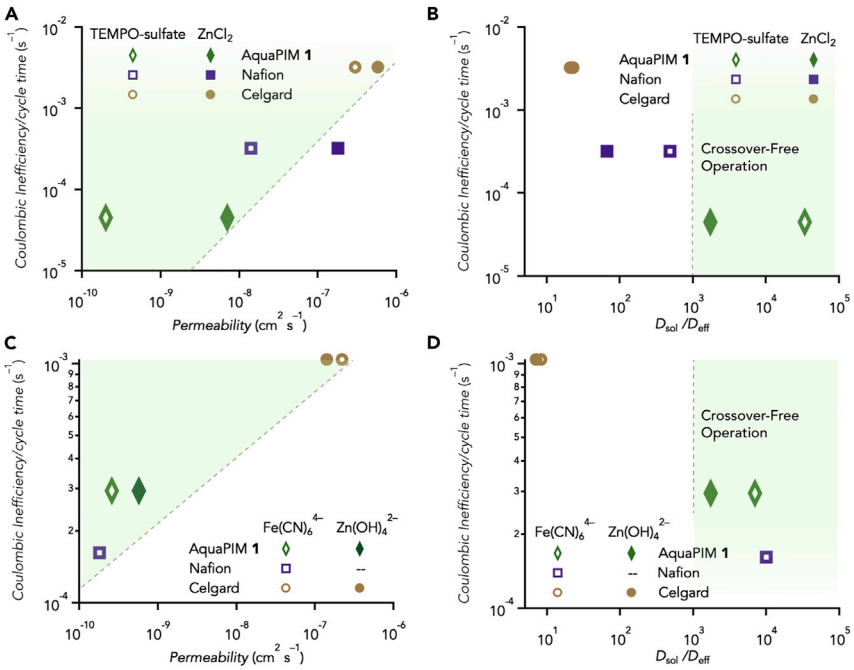

Figure 9. Comparative Evaluation of Membrane Properties and Coulombic Inefficiency and Cycle Time Degradation Rates Observed for Different Cell Chemistries

(A and B) Permeability versus the quotient of Coulombic inefficiency and cycle time (A) and D_{sol}/D_{eff} versus the quotient of Coulombic inefficiency and cycle time (B) for Zn–TEMPO-sulfate cells reported in Figure 7.

(C and D) Permeability versus the quotient of Coulombic inefficiency and cycle time (C) and D_{sol}/D_{eff} versus the quotient of Coulombic inefficiency and cycle time (D) for Zn–$K_4Fe(CN)_6$ cells reported in Figure 8.

comparable $K_4Fe(CN)_6$ blocking ability, we hypothesized that Zn–$K_4Fe(CN)_6$ cells (~1.74 V) could perform similarly well for cells configured with either AquaPIM **1** or Nafion 212 membranes and that each of these should outperform cells configured with non-blocking Celgard 3501 separators. To test these hypotheses, we assembled 8 mAh-capacity Zn–$K_4Fe(CN)_6$ cells (Figure 8) consisting of a Zn anode, a 175 mM $Na_2Zn(OH)_4$ anolyte in 5.0 M NaOH, any one of the three membranes under consideration, a 35 mM $K_4Fe(CN)_6$ catholyte in 5.0 M NaOH, and a reticulated vitreous carbon current collector. All cells were cycled at 25°C at a rate of C/4. The AquaPIM **1** cell attained the highest initial capacity, 65% of theoretical, and maintained 95% of this initial capacity over 60 cycles spanning 13 days (0.13% loss per cycle) with a Coulombic efficiency ~95% throughout cycling. The Nafion 212 performed nearly, but not quite, as well, reaching 60% of its theoretical capacity initially, and over 60 cycles spanning 8.75 days, maintaining 80% of that initial capacity (0.38% loss per cycle) with a Coulombic efficiency of ~98%. In contrast, as expected, given the $D_{sol}/D_{eff} < 10^3$ for both active materials, the cell configured with Celgard 3501 showed 2.2% capacity fade per cycle, with only 47% capacity retention over 24 cycles. Furthermore, only 52% of the theoretical capacity was accessed in the first cycle and the Coulombic efficiency was consistently lower (~90%). As was noted previously, plotting the quotient of the Coulombic inefficiency and cumulative cycle time for each cell against either the absolute permeability or D_{sol}/D_{eff} for each active material and a given membrane (Figure 8), we again conclude that cell performance tracks active-material permeability, inversely, and that to achieve a stable cycling outcome requires $D_{sol}/D_{eff} > 10^3$ for both active materials.

In each of the examples above, the chosen cell chemistries afforded $D_{sol}/D_{eff} > 10^3$ for both active materials in the cell for at least one of the membranes, most consistently for AquaPIM **1**. However, we did not yet consider a cell chemistry for which only one of the actives falls above the 10^3 threshold for D_{sol}/D_{eff}. To resolve this outstanding question, we investigated an 8 mAh-capacity Zn–Na_2S_4 cell (Figure S31) assembled with a Zn anode, an anolyte consisting of 70 mM $Na_2Zn(OH)_4$ in 1.0 M NaOH, an AquaPIM **1** membrane, a catholyte consisting of 5.8 mM Na_2S_4 in 1.0 M NaOH, and a reticulated vitreous carbon current collector. In such a cell, the AquaPIM **1** membrane can be expected to block zincate crossover effectively ($D_{sol}/D_{eff} = 1.7 \times 10^3$) but to an extent permits polysulfide crossover ($D_{sol}/D_{eff} = 1.3 \times 10^2$). The crossover of polysulfides in such cells could lead to the formation of zinc sulfide either in the anolyte or on the Zn electrode, if left unchecked. Complete passivation of the Zn electrode by ionically-insulating ZnS would render it inoperable, which would prevent the cell from functioning. Indeed, after cell assembly, only 1% of the 8 mAh theoretical capacity was accessed in the initial cycle, fading to 0.6% of the theoretical capacity after 100 cycles. Cyclic voltammetry of the catholyte (Figure S31) revealed a shift in cathodic peak to higher potential, indicative of smaller polysulfides crossing over to the anode. Concomitantly, we observed the formation of a precipitate on the zinc metal anode, which we concluded was ZnS after analysis by x-ray diffraction (XRD) (Figure S31). The poor performance of the Zn–Na_2S_4 cell supports our conclusion that D_{sol}/D_{eff} must be greater than 10^3 for both active materials in the cell for a given cell chemistry, electrolyte, and choice of membrane to anticipate stable, crossover-free operation.

Design Rules Collectively Evidenced

The design rules laid out here serve as a guide for how to pair selective membranes and active materials in aqueous electrochemical cells to avoid active-material crossover and minimize membrane area-specific resistance (ASR) and deleterious side reactions. Regarding the membrane, we identify constraints in 2D versus 3D polymer design needed to provide gains in ionic conductivity over commercial membranes, such as Nafion 212, at the extremes of electrolyte alkalinity, without sacrificing chemomechanical properties. We also identify the extent to which AquaPIM membrane architectures, optimized for stability and conductivity, are able to block the crossover of organic and inorganic active materials that are potential candidates for grid batteries. Our evaluation of these characteristics alongside those for commercial membranes led us to codify a figure of merit, D_{sol}/D_{eff}, which captures the intrinsic blocking character of any membrane with a specific active material. We then show how membrane transport selectivity dictates cell cycle life and overall efficiency. Specifically, we evaluated the cell performance for a variety of cell chemistries and membranes. We find that the Coulombic inefficiency and the cycle life of alkaline electrochemical cells is inversely correlated (i.e., ~linear) with the membrane figure of merit, D_{sol}/D_{eff}, for the active materials of the electrochemical cells (Figure 9). Post-mortem analysis further indicates that when $D_{sol}/D_{eff} > 10^3$ for both active materials for a given membrane, there is no observable crossover over a period of at least two weeks of continuous operation.

The significance of this is that we have only to measure the simple membrane figure of merit in a diffusion cell in order to predict the lifetime and efficiency of the electrochemical cell were that membrane in place—knowledge that would have otherwise required intensive and resource consuming experimentation to acquire. As such, it should be possible from our design rules to more rapidly screen membranes generally, for alkaline batteries prone to crossover issues, now that we have a lower limit for D_{sol}/D_{eff} in order for that membrane to have prospects for crossover-free

operation. We anticipate that researchers interested in any battery chemistry can construct similar plots to scout for membranes suitable for use in those cells. Analogous plots, initially conceived by Robeson for understanding polymer membrane performance in gas separations, brought a sense of purpose to that field by recognizing upper bounds for gas permeability and selectivity.[76–79] The field of energy storage has lacked such clarity for design rules tying membrane transport selectivity to cell performance. Our work endeavors to resolve this gap and welcomes other researchers to use their own results to enrich the datasets from which our understanding of electrochemical upper bounds are based, so as to collectively advance toward our collective goal of grid modernization through well-integrated and scalable electrochemical energy storage.

Conclusion

Aqueous electrochemical devices requiring highly conductive, ion-selective cation exchange membranes see impressive gains when configured with AquaPIM membranes, which utilize exceptionally rigid microporous architectures and high-pH stable, ionizable amidoxime pore functionality to enforce transport selectivity. Within this architectural framework, we showed that membrane processing and performance was controlled at the molecular level by the varying structure of the monomer's contortion site, whether in 2D or 3D. With this control, we identified a specific membrane architecture from which a variety of Zn-based electrochemical cells, including aqueous Zn–TEMPO-sulfate and Zn–$K_4Fe(CN)_6$ cells, were remarkably stable. We further demonstrated a threshold value for transport selectivity met by such membranes in order for crossover-free operation to materialize; once realized, we further tied this transport selectivity to extended cycle life and higher round-trip energy efficiency. These design rules are likely to apply to other AquaPIM variants and microporous polymer analogs in both static and flow systems, for the breadth of aqueous cell chemistries currently under investigation[80–86] for redox-flow batteries, hybrid redox-flow batteries, redox-targeting batteries, and solar flow batteries, including metal coordination complexes, organometallics, polyoxometalates, redox-active organic molecules, and redoxmers. For the specific demonstration by AquaPIM **1** for exceptional zincate blocking under highly alkaline conditions, we anticipate that these membranes may also advance the designs of Zn–O_2, Zn–MnO_2, and Zn–MOF batteries.[87–91] However, further manipulations to AquaPIM membrane architectures are required for smaller active materials, particularly inorganics such as polysulfides or halides. With more diversity-oriented chemistries for PIMs on the horizon,[2] this longer-term challenge may be addressable sooner rather than later.

EXPERIMENTAL PROCEDURES

Small-molecule simulations as well as polymer synthesis, characterization, processing, transport measurements, cell assembly, and post-mortem analysis of cell components are provided in the Supplemental Information.

SUPPLEMENTAL INFORMATION

Supplemental Information can be found online at https://doi.org/10.1016/j.joule.2019.08.025.

ACKNOWLEDGMENTS

This work was supported by the Joint Center for Energy Storage Research (JCESR), an Energy Innovation Hub funded by the U.S. Department of Energy, Office of Science, Office of Basic Energy Sciences. Portions of this work, including polymer

synthesis and characterization, were carried out as a user project at the Molecular Foundry, which is supported by the Office of Science, Office of Basic Energy Sciences of the U.S. Department of Energy under contract no. DE-AC02-05CH11231. S.M.M. and M.E.C. acknowledge support from the Center for Gas Separations Relevant to Clean Energy Technologies, an Energy Frontier Research Center funded by the U.S. Department of Energy, Office of Science, Basic Energy Sciences under award # DE-SC0001015 to carry out gas sorption and GIWAXS measurements on AquaPIMs. GIWAXS measurements were carried out at the Advanced Light Source, which is a DOE Office of Science User Facility under contract no. DE-AC02-05CH11231. Computation was carried out at the National Energy Research Scientific Computing Center (NERSC), a U.S. Department of Energy Office of Science User Facility operated under the same contract.

AUTHOR CONTRIBUTIONS

B.A.H. designed and directed the project. M.J.B., S.S., and L.M. synthesized the AquaPIMs. M.J.B., M.N.B., S.S., S.M.M., L.L., L.M., M.E.C., and Y.-M.C., carried out the polymer characterization, membrane processing, and detailed characterization of membrane stability and transport properties. M.J.B. conducted cell assembly and testing as well as post-mortem analysis of cell components. A.B. and D.P. contributed all molecular simulations. M.J.B. and B.A.H. wrote the manuscript with contributions from all co-authors.

DECLARATION OF INTERESTS

B.A.H., S.S., M.J.B., M.N.B., M.E.C., and S.M.M. are inventors on US provisional patent application 62/719,498 submitted by Lawrence Berkeley National Laboratory, which covers AquaPIMs, as well as aspects of their use.

Received: November 16, 2018
Revised: December 31, 2018
Accepted: August 30, 2019
Published: October 9, 2019

REFERENCES

1. Ye, Y., and Elabd, Y.A. (2012). Chemical stability of anion exchange membranes for alkaline fuel cells. In Polym. Energy Storage Deliv.: Polyelectrolytes Batteries Fuel Cells, K.A. Page, C.L. Soles, and J. Runt, eds. (American Chemical Society), pp. 233–251.

2. Li, C., Meckler, S.M., Smith, Z.P., Bachman, J.E., Maserati, L., Long, J.R., and Helms, B.A. (2018). Engineered transport in microporous materials and membranes for clean energy technologies. Adv. Mater *30*, 1704953.

3. Yuan, Z., Zhang, H., and Li, X. (2018). Ion conducting membranes for aqueous flow battery systems. Chem. Commun. (Camb.) *54*, 7570–7588.

4. Kusoglu, A., and Weber, A.Z. (2013). Degradation induced changes in structure–property relationship of Perfluorosulfonic-acid (PFSA) membranes. ECS Trans. *58*, 999–1003.

5. Kreuer, K.-D. (2014). Ion conducting membranes for fuel cells and other electrochemical devices. Chem. Mater *26*, 361–380.

6. Sun, Z., Pan, J., Guo, J., and Yan, F. (2018). The alkaline stability of anion exchange membrane for fuel cell applications: the effects of alkaline media. Adv. Sci. *5*, 1800065.

7. Low, Z.X., Budd, P.M., McKeown, N.B., and Patterson, D.A. (2018). Gas permeation properties, physical aging, and its mitigation in high free volume glassy polymers. Chem. Rev. *118*, 5871–5911.

8. Hirotsu, T., Katoh, S., Sugasaka, K., Sen Obar, M., and Itagaki, T. (1986). Binding properties of polymer having amidoxime groups with proton and metal ions. Sep. Sci. Technol *21*, 1101–1110.

9. Nilchi, A., Babalou, A.A., Rafiee, R., and Sid Kalal, H. (2008). Adsorption properties of amidoxime resins for separation of metal ions from aqueous systems. React. Funct. Polym *68*, 1665–1670.

10. Patel, H.A., and Yavuz, C.T. (2012). Noninvasive functionalization of polymers of intrinsic microporosity for enhanced CO_2 capture. Chem. Commun. (Camb.) *48*, 9989–9991.

11. Budd, P.M., Mckeown, N.B., Ghanem, B.S., Msayib, K.J., Fritsch, D., Starannikova, L., Belov, N., Sanfirova, O., Yampolskii, Y., and Shantarovich, V. (2008). Gas permeation parameters and other physiochemical properties of a polymer of intrinsic microporosity: polybenzodioxane PIM-1. J. Membr. Sci. *325*, 851–860.

12. Zhang, J., Jin, J., Cooney, R., Fu, Q., Qiao, G.G., Thomas, S., and Merkel, T.C. (2015). Synthesis of perfectly alternating copolymers for polymers of intrinsic microporosity. Polym. Chem. *6*, 5003–5008.

13. Winsberg, J., Stolze, C., Schwenke, A., Muench, S., Hager, M.D., and Schubert, U.S. (2017). Aqueous 2,2,6,6-tetramethylpiperidine-*N*-oxyl catholytes for a high-capacity and high current density oxygen-insensitive hybrid-flow battery. ACS Energy Lett. *2*, 411–416.

14. Yuan, Z., Duan, Y., Liu, T., Zhang, H., and Li, X. (2018). Toward a low-cost alkaline zinc–iron flow battery with a polybenzimidazole custom membrane for stationary energy storage. iScience *3*, 40–49.

15. Gross, M.M., and Manthiram, A. (2018). Rechargeable zinc–aqueous polysulfide battery with a mediator-ion solid electrolyte. ACS Appl. Mater. Interfaces *10*, 10612–10617.

16. Arora, P., and Zhang, Z.J. (2004). Battery separators. Chem. Rev. *104*, 4419–4462.

17. Kyu, T. (1985). Structure and properties of perfluorinated ion-exchange membranes. In Materials Science of Synthetic, L.D.R. Membranes, ed. (American Chemical Society), pp. 365–405.

18. Kusoglu, A., and Weber, A.Z. (2017). New insights into perfluorinated sulfonic-acid ionomers. Chem. Rev. *117*, 987–1104.

19. Li, Z., Pan, M.S., Su, L., Tsai, P.-C., Badel, A.F., Valle, J.M., Eiler, S.L., Xiang, K., Brushett, F.R., and Chiang, Y.-M. (2017). Air-breathing aqueous sulfur flow battery for ultralow-cost long-duration electrical storage. Joule *1*, 306–327.

20. Zhang, J., Jiang, G., Xu, P., Ghorbani Kashkooli, A.G., Mousavi, M., Yu, A., and Chen, Z. (2018). An all-aqueous redox flow battery with unprecedented energy density. Energy Environ. Sci. *11*, 2010–2015.

21. Gong, K., Ma, X., Conforti, K.M., Kuttler, K.J., Grunewald, J.B., Yeager, K.L., Bazant, M.Z., Gu, S., and Yan, Y. (2015). A zinc–iron redox-flow battery under $100 per kW h of system capital cost. Energy Environ. Sci. *8*, 2941–2945.

22. Gong, K., Xu, F., Grunewald, J.B., Ma, X., Zhao, Y., Gu, S., and Yan, Y. (2016). All-soluble all-iron aqueous redox-flow battery. ACS Energy Lett. *1*, 89–93.

23. Li, B., Liu, J., Nie, Z., Wang, W., Reed, D., Liu, J., McGrail, P., and Sprenkle, V. (2016). Metal organic frameworks as highly active electrocatalysts for high-energy density, aqueous zinc–polyiodide redox flow batteries. Nano Lett. *16*, 4335–4340.

24. Beh, E.S., De Porcellinis, D., Gracia, R.L., Xia, K.T., Gordon, R.G., and Aziz, M.J. (2017). A neutral pH aqueous organic–organometallic redox flow battery with extremely high capacity retention. ACS Energy Lett. *2*, 639–644.

25. Hu, B., DeBruler, C., Rhodes, Z., and Liu, T.L. (2017). Long-cycling aqueous organic redox flow battery (AORFB) toward sustainable and safe energy storage. J. Am. Chem. Soc. *139*, 1207–1214.

26. Pratt, H.D., Hudak, N.S., Fang, X., and Anderson, T.M. (2013). A polyoxometalate flow battery. J. Power Sources *236*, 259–264.

27. Friedl, J., Holland-Cunz, M.V., Cording, F., Pfanschilling, F.L., Wills, C., McFarlane, W., Schricker, B., Fleck, R., Wolfschmidt, H., and Stimming, U. (2018). Asymmetric polyoxometalate electrolytes for advanced flow batteries. Energy Environ. Sci. *11*, 3010–3018.

28. VanGelder, L.E., Kosswattaarachchi, A.M., Forrestel, P.L., Cook, T.R., and Matson, E.M. (2018). Polyoxovanadate-alkoxide clusters as multi-electron charge carriers for symmetric non-aqueous redox flow batteries. Chem. Sci. *9*, 1692–1699.

29. Huskinson, B., Marshak, M.P., Suh, C., Er, S., Gerhardt, M.R., Galvin, C.J., Chen, X., Aspuru-Guzik, A., Gordon, R.G.A., and Aziz, M.J. (2014). A metal-free organic-inorganic aqueous flow battery. Nature *505*, 195–198.

30. Lin, K., Chen, Q., Gerhardt, M.R., Tong, L., Kim, S.B., Eisenach, L., Valle, A.W., Hardee, D., Gordon, R.G., Aziz, M.J., et al. (2015). Alkaline quinone flow battery. Science *349*, 1529–1532.

31. Liu, T., Wei, X., Nie, Z., Sprenkle, V., and Wang, W. (2015). A total organic aqueous redox flow battery employing low cost and sustainable methyl viologen (MV) anolyte and 4-HO-TEMPO catholyte. Adv. Energy Mater. *6*, 1501449.

32. DeBruler, C., Hu, B., Moss, J., Liu, X., Luo, J., Sun, Y., and Liu, T.L. (2017). Designer two-electron storage viologen anolyte materials for neutral aqueous organic redox flow batteries. Chem *3*, 961–978.

33. Yang, Z., Tong, L., Tabor, D.P., Beh, E.S., Goulet, M.-A., De Porcellinis, D., Aspuru-Guzik, A., Gordon, R.G., and Aziz, M.J. (2018). Alkaline benzoquinone aqueous flow battery for large-scale storage of electrical energy. Adv. Energy Mater *8*, 1870034.

34. Hollas, A., Wei, X., Murugesan, V., Nie, Z., Li, B., Reed, D., Liu, J., Sprenkle, V., and Wang, W. (2018). A biomimetic high-capacity phenazine-based anolyte for aqueous organic redox flow batteries. Nat. Energy *3*, 508–514.

35. Luo, J., Hu, B., DeBruler, C., and Liu, T.L. (2018). A π-conjugation extended viologen as a two-electron storage anolyte for total organic aqueous redox flow batteries. Angew. Chem. Int. Ed. Engl. *57*, 231–235.

36. Kwabi, D.G., Lin, K., Ji, Y., Kerr, E.F., Goulet, M.-A., De Porcellinis, D., Tabor, D.P., Pollack, D.A., Aspuru-Guzik, A., Gordon, R.G., et al. (2018). Alkaline quinone flow battery with Long lifetime at pH 12. Joule *2*, 1894–1906.

37. Gorman, C. (1998). Metallodendrimers: structural diversity and functional behavior. Adv. Mater *10*, 295–309.

38. Ong, W., and Kaifer, A.E. (2002). Unusual electrochemical properties of unsymmetric viologen dendrimers. J. Am. Chem. Soc. *124*, 9358–9359.

39. Nagarjuna, G., Hui, J., Cheng, K.J., Lichtenstein, T., Shen, M., Moore, J.S., and Rodríguez-López, J. (2014). Impact of redox active polymer molecular weight on the electrochemical properties and transport across porous separators in non-aqueous solvents. J. Am. Chem. Soc. *136*, 16309–16316.

40. Janoschka, T., Martin, N., Martin, U., Friebe, C., Morgenstern, S., Hiller, H., Hager, M.D., and Schubert, U.S. (2015). An aqueous, polymer-based redox-flow battery using non-corrosive, safe, and low-cost materials. Nature *527*, 78–81.

41. Doris, S.E., Ward, A.L., Baskin, A., Frischmann, P.D., Gavvalapalli, N., Chénard, E., Sevov, C.S., Prendergast, D., Moore, J.S., and Helms, B.A. (2017). Macromolecular design strategies for preventing active-material crossover in non-aqueous all-organic redox-flow batteries. Angew. Chem. Int. Ed. Engl. *56*, 1595–1599.

42. Hendriks, K.H., Robinson, S.G., Braten, M.N., Sevov, C.S., Helms, B.A., Sigman, M.S., Minteer, S.D., and Sanford, M.S. (2018). High-performance oligomeric catholytes for effective macromolecular separation in nonaqueous redox flow batteries. ACS Cent. Sci. *4*, 189–196.

43. Baran, M.J., Braten, M.N., Montoto, E.C., Gossage, Z.T., Ma, L., Chénard, E., Moore, J.S., Rodríguez-López, J., and Helms, B.A. (2018). Designing redox-active oligomers for crossover-free, non-aqueous redox-flow batteries with high volumetric energy density. Chem. Mater. *30*, 3861–3866.

44. Friedl, J., Lebedeva, M.A., Porfyrakis, K., Stimming, U., and Chamberlain, T.W. (2018). All-fullerene-based cells for nonaqueous redox flow batteries. J. Am. Chem. Soc. *140*, 401–405.

45. Skyllas-Kazacos, M., Chakrabarti, M.H., Hajimolana, S.A., Mjalli, F.S., and Saleem, M. (2011). Progress in flow battery research and development. J. Electrochem. Soc. *158*, R55–R79.

46. Neamţu, G.N., Airinei, A., and Brum, M. (1980). Study of the stability of some imide type polymers in alkaline media. Angew. Makromol. Chemie *90*, 37–45.

47. Chen, D., and Hickner, M.A. (2012). Degradation of imidazolium- and quaternary ammonium-functionalized poly(fluorenyl ether ketone sulfone) anion exchange membranes. Aca Appl. Mater. Interfaces *4*, 5775–5781.

48. Hugar, K.M., Kostalik, H.A., IV, and Coates, G.W. (2015). Imidazolium cations with exceptional alkaline stability: a systematic study of structure−stability relationships. J. Am. Chem. Soc. *137*, 8730–8737.

49. Mehio, N., Lashely, M.A., Nugent, J.W., Tucker, L., Correia, B., Do-Thanh, C.L., Dai, S., Hancock, R.D., and Bryantsev, V.S. (2015). Acidity of the amidoxime functional group in aqueous solution: a combined experimental and computational study. J. Phys. Chem. B *119*, 3567–3576.

50. Mehio, N., Williamson, B., Oyola, Y., Mayes, R.T., Janke, C., Brown, S., and Dai, S. (2016). Acidity of the poly(acrylamidoxime) adsorbent in aqueous solution: determination of the proton affinity distribution via potentiometric titrations. Ind. Eng. Chem. Res. *55*, 4217–4223.

51. Das, S., Tsouris, C., Zhang, C., Kim, J., Brown, S., Oyola, Y., Janke, C.J., Mayes, R.T., Kuo, L.-J., Wood, J.R., et al. (2016). Enhancing uranium uptake by amidoxime adsorbent in seawater: an investigation for optimum alkaline conditioning parameters. Ind. Eng. Chem. Res. *55*, 4294–4302.

52. McKeown, N.B., and Budd, P.M. (2010). Exploitation of intrinsic microporosity in polymer-based materials. Macromolecules *43*, 5163–5176.

53. McKeown, N.B., and Budd, P.M. (2006). Polymers of intrinsic microporosity (PIMs): organic materials for membrane separations, heterogeneous catalysis and hydrogen storage. Chem. Soc. Rev. *35*, 675–683.

54. Li, C., Ward, A.L., Doris, S.E., Pascal, T.A., Prendergast, D., and Helms, B.A. (2015). Polysulfide-blocking microporous polymer membrane tailored for hybrid Li–sulfur flow batteries. Nano Lett. *15*, 5724–5729.

55. Doris, S.E., Ward, A.L., Frischmann, P.D., Li, L., and Helms, B.A. (2016). Understanding and controlling the chemical evolution and polysulfide- blocking ability of lithium–sulfur battery membranes cast from polymers of intrinsic microporosity. J. Mater. Chem. A *4*, 16946–16952.

56. Ward, A.L., Doris, S.E., Li, L., Hughes, M.A., Qu, X., Persson, K.A., and Helms, B.A. (2017). Materials genomics screens for adaptive ion transport behavior by redox- switchable microporous polymer membranes in lithium-sulfur batteries. ACS Cent. Sci. *3*, 399–406.

57. Rose, I., Bezzu, C.G., Carta, M., Comesaña-Gándara, B., Lasseuguette, E., Ferrari, M.C., Bernardo, P., Clarizia, G., Fuoco, A., Jansen, J.C., et al. (2017). Polymer ultrapermeability from the inefficient packing of 2D chains. Nat. Mater *16*, 932–937.

58. Hexemer, A., Bras, W., Glossinger, J., Schaible, E., Gann, E., Kirian, R., MacDowell, A., Church, M., Rude, B., and Padmore, H. (2010). A SAXS/WAXS/GISAXS beamline with multilayer monochromator. J. Phys.: Conf. Ser. *247*, 012007.

59. McDermott, A.G., Budd, P.M., McKeown, N.B., Colina, C.M., and Runt, J. (2014). Physical aging of polymers of intrinsic microporosity: a SAXS/WAXS study. J. Mater. Chem. A *2*, 11742–11752.

60. McDermott, A.G., Larsen, G.S., Budd, P.M., Colina, C.M., and Runt, J. (2011). Structural characterization of a polymer of intrinsic microporosity: X-ray scattering with interpretation enhanced by Molecular Dynamics simulations. Macromolecules *44*, 14–16.

61. Emmler, T., Heinrich, K., Fritsch, D., Budd, P.M., Chaukura, N., Ehlers, D., Rätzke, K., and Faupel, F. (2010). Free volume investigation of polymers of intrinsic microporosity (PIMs): PIM-1 and PIM1 copolymers incorporating Ethanoanthracene units. Macromolecules *43*, 6075–6084.

62. Yin, H., Chua, Y.Z., Yang, B., Schick, C., Harrison, W.J., Budd, P.M., Böhning, M., and Schönhals, A. (2018). First clear-cut experimental evidence of a glass transition in a polymer with intrinsic microporosity: PIM-1. J. Phys. Chem. Lett. *9*, 2003–2008.

63. Clark, T.J., Robertson, N.J., Kostalik, H.A.I.V., Lobkovsky, E.B., Mutolo, P.F., Abruña, H.D., and Coates, G.W. (2009). A ring-opening metathesis polymerization route to alkaline anion exchange membranes: development of hydroxide-conducting thin films from an ammonium-functionalized monomer. J. Am. Chem. Soc. *131*, 12888–12889.

64. Hibbs, M.R., Fujimoto, C.H., and Cornelius, C.J. (2009). Synthesis and characterization of poly(phenylene)-based anion exchange membranes for alkaline fuel cells. Macromolecules *42*, 8316–8321.

65. Kostalik, H.A.I.V., Clark, T.J., Robertson, N.J., Mutolo, P.F., Longo, J.M., Abruña, H.D., and Coates, G.W. (2010). Solvent processable tetraalkylammonium-functionalized polyethylene for use as an alkaline anion exchange membrane. Macromolecules *43*, 7147–7150.

66. Noonan, K.J.T., Hugar, K.M., Kostalik, H.A.I.V., Lobkovsky, E.B., Abruña, H.D., and Coates, G.W. (2012). Phosphonium-functionalized polyethylene: a new class of base-stable alkaline anion exchange membranes. J. Am. Chem. Soc. *134*, 18161–18164.

67. He, G., Li, Z., Zhao, J., Wang, S., Wu, H., Guiver, M.D., and Jiang, Z. (2015). Nanostructured ion-exchange membranes for fuel cells: recent advances and perspectives. Adv. Mater *27*, 5280–5295.

68. Yang, Z., Guo, R., Malpass-Evans, R., Carta, M., McKeown, N.B., Guiver, M.D., Wu, L., and Xu, T. (2016). Highly conductive anion-exchange membranes from microporous Tröger's base polymers. Angew. Chem. Int. Ed. Engl. *55*, 11499–11502.

69. Zhang, K., McDonald, M.B., Genina, I.E.A., and Hammond, P.T. (2018). A highly conductive and mechanically robust OH^- conducting membrane for alkaline water electrolysis. Chem. Mater. *30*, 6420–6430.

70. DePorcellinis, D., Mecheri, B., D'Epifanio, A., Licoccia, S., Granados-Focil, S., and Aziz, M.J. (2018). Sulfonated poly(ether ether ketone) as cation exchange membrane for alkaline redox flow batteries. J. Electrochem. Soc. *165*, A1137–A1139.

71. Zawodzinski, T.A., Derouin, C., Radzinski, S., Sherman, R.J., Smith, V.T., Springer, T.E., and Gottesfeld, S. (1993). Water uptake by and transport through nafion 117 membranes. J. Electrochem. Soc. *140*, 1041–1047.

72. Peng, J., Lou, K., Goenaga, G., and Zawodzinski, T. (2018). Transport properties of perfluorosulfonate membranes ion exchanged with cations. ACS Appl. Mater. Interfaces *10*, 38418–38430.

73. Kamcev, J., Paul, D.R., and Freeman, B.D. (2018). Equilibrium ion partitioning between aqueous salt solutions and inhomogeneous ion exchange membranes. Desalination *446*, 31–41.

74. Zhang, H., Xu, W., Yuan, Z., and Li, X. (2018). Mechanism and transfer behavior of ions in nafion membranes under alkaline media. J. Mem. Sci. *566*, 8–14.

75. Tung, S.O., Fisher, S.L., Kotov, N.A., and Thompson, L.T. (2018). Nanoporous aramid nanofibre separators for nonaqueous redox flow batteries. Nat. Commun. *9*, 4193.

76. Park, H.B., Kamcev, J., Robeson, L.M., Elimelech, M., and Freeman, B.D. (2017). Maximizing the right stuff: the trade-off between membrane permeability and selectivity. Science *356*, eaab0530.

77. Robeson, L.M. (1991). Correlation of separation factor versus permeability for polymeric membranes. J. Membr. Sci. *62*, 165–185.

78. Freeman, B.D. (1999). Basis of permeability/selectivity tradeoff relations in polymeric gas separation membranes. Macromolecules *32*, 375–380.

79. Robeson, L.M. (2008). The upper bound revisited. J. Membr. Sci. *320*, 390–400.

80. Yan, R., and Wang, Q. (2018). Redox-targeting-based flow batteries for large-scale energy storage. Adv. Mater. *30*, e1802406.

81. Zhou, M., Huang, Q., Pham Truong, T.N.P., Ghilane, J., Zhu, Y.G., Jia, C., Yan, R., Fan, L., Randriamahazaka, H., and Wang, Q. (2017). Nernstian-potential-driven redox-targeting reactions of battery materials. Chem *3*, 1036–1049.

82. Yu, J., Fan, L., Yan, R., Zhou, M., and Wang, Q. (2018). Redox targeting-based aqueous redox flow lithium battery. ACS Energy Lett. *3*, 2314–2320.

83. Wedege, K., Bae, D., Smith, W.A., Mendes, A., and Bentien, A. (2018). Solar redox flow batteries with organic redox couples in aqueous electrolytes: a minireview. J. Phys. Chem. C *122*, 25729–25740.

84. Yu, M., McCulloch, W.D., Beauchamp, D.R., Huang, Z., Ren, X., and Wu, Y. (2015). Aqueous lithium–iodine solar flow battery for the simultaneous conversion and storage of solar energy. J. Am. Chem. Soc. *137*, 8332–8335.

85. McKone, J.R., DiSalvo, F.J., and Abruña, H.D. (2017). Solar energy conversion, storage, and release using an integrated solar-driven redox flow battery. J. Mater. Chem. A *5*, 5362–5372.

86. Li, W., Fu, H.-C., Zhao, Y., He, J.-H., and Jin, S. (2018). 14.1% efficient monolithically integrated solar flow battery. Chem *4*, 2644–2657.

87. Li, Y., and Dai, H. (2014). Recent advances in zinc–air batteries. Chem. Soc. Rev. *43*, 5257–5275.

88. Hertzberg, B.J., Huang, A., Hsieh, A., Chamoun, M., Davies, G., Seo, J.K., Zhong, Z., Croft, M., Erdonmez, C., Meng, Y.S., et al. (2016). Effect of multiple cation electrolyte mixtures on rechargeable Zn−MnO_2 alkaline battery. Chem. Mater *28*, 4536–4545.

89. Yadav, G.G., Gallaway, J.W., Turney, D.E., Nyce, M., Huang, J., Wei, X., and Banerjee, S. (2017). Regenerable Cu-intercalated MnO_2 layered cathode for highly cyclable energy dense batteries. Nat. Commun. *8*, 14424.

90. Turney, D.E., Gallaway, J.W., Yadav, G.G., Ramirez, R., Nyce, M., Banerjee, S., Chen-Wiegart, Y.K., Wang, J., D'Ambrose, M.J., Kolhekar, S., et al. (2017). Rechargeable zinc alkaline anodes for long-cycle energy storage. Chem. Mater *29*, 4819–4832.

91. Hurlbutt, K., Wheeler, S., Capone, I., and Pasta, M. (2018). Prussian Blue analogs as battery materials. Joule *2*, 1950–1960.